Journal of Nanobiotechnology

RESEARCH

Open Access

Single-cell in situ mapping of glioblastoma and astrocyte cell lines treated with a carbon dot–mediated riluzole nanotherapeutic agent: a live-cell μFTIR and soft X-ray tomography approach

Tanja Dučić[1*], Eva Pereiro[1], Milena Ninkovic[2], Swetlana Sperling[2], Veit Rohde[2], Claudia Fernández-González[1], Manuel Algarra[3] and Elena González-Muñoz[4,5*]

Abstract

Nanoparticle-based drug carriers offer a promising alternative to conventional cancer therapies by enabling targeted delivery and reducing off-target toxicity. Here, we used synthesised and characterised carbon-based nanoparticles derived from 2-acrylamido-2-methylpropanesulfonic acid (AMPS-CDs), demonstrating biocompatibility with both human astrocytes and glioblastoma cells. We assessed their potential to enhance riluzole's efficacy through synergistic interaction (AMPS-CDs@RZ) using live-cell synchrotron-based FTIR spectroscopy and cryo-soft X-ray tomography to monitor biochemical and structural changes at the single-cell level. While AMPS-CDs nanoparticles alone were non-toxic, the combination with riluzole significantly enhanced cell death in glioblastoma cells, with a significantly lower impact in non-cancerous astrocytes. Treatment with AMPS-CDs@RZ induced significant changes in bio-macromolecules, including DNA, protein conformation, and lipid metabolism. Notably, the treatment triggered nuclear envelope (NE) blebbing in glioblastoma cells, likely due to the interaction of the nanoparticle formulation with the nuclear membrane. This initiated stress signals that disrupted the cell's inner intracellular membrane system, including the endoplasmic reticulum and mitochondria. To our knowledge, this is the first report linking NE blebbing to this mechanism involving membrane disassembly and nuclear envelope blebbing in riluzole-induced toxicity in glioblastoma is novel, providing a new therapeutic strategy and insights into cellular stress responses. These findings suggest that AMPS-CDs nanoparticles are a promising carrier for riluzole, potentially enhancing the specificity and efficacy of glioblastoma treatments while minimising damage to healthy tissues.

Keywords Riluzole, Carbon dots, Nano-carrier, Glioblastoma, Astrocytes, FTIR, Soft x-ray tomography

*Correspondence:
Tanja Dučić
tducic@cells.es
Elena González-Muñoz
egonmu@uma.es

Full list of author information is available at the end of the article

Introduction

Glioblastoma multiforme (GBM) is a highly aggressive brain tumor originating from transformed astrocytes [1] and classified as grade IV glioma by the World Health Organisation (WHO) [2]. Despite its high tumor-related mortality rate, advancements in chemotherapy and cancer genomics provide hope for improving survival rates [3, 4]. While the genetic makeup of cells dictates their potential for uncontrolled proliferation, the actual occurrence of proliferation depends on the availability of organic compounds and trace elements within the cells [5]. Recent progress in nanoscience offers promising opportunities for developing new drug delivery systems that enhance the efficiency of therapeutic agents.

Nanochemistry is currently playing a critical role in this effort by developing various nanoparticles as a carrier for drug compositions [6]. These nano-delivery systems are designed to selectively deliver drugs to different types of cancer cells, minimising damage to healthy cells and increasing treatment efficacy. Previously, we synthesised and characterised carbon dot nanoparticles based on 2-acrylamido-2-methylpropanesulfonic acid (AMPS-CDs), which demonstrated biocompatibility with glioblastoma tissue [7]. Furthermore, we tested this nanoparticle as a nanocarrier system for the drug riluzole (RZ) [7]a drug approved by the Food and Drug Administration (FDA) for the treatment of amyotrophic lateral sclerosis (ALS) [8]. Riluzole [2-amino-6 (trifluoromethoxy)benzothiazole] inhibits glutamate release into the synaptic cleft and exhibits antineoplastic properties against various cancers, including melanoma, glioma, breast, and prostate cancer, by reducing glutamate levels [9]. Additionally, riluzole has been shown to enhance the response of cancer cells to chemotherapy and radiotherapy [10–12]. In our previous work, the AMPS-CDs@RZ nanoparticle demonstrated effectiveness in promoting cell death in a GBM patient-derived cell line [7].

In this study, we conducted a comparative analysis of GBM cells and a healthy human astrocyte cell Line to explore subtle differences in biologically relevant molecules in live cells. Considering that astrocyte cells make up approximately 50% of the brain's total cell population and play a key role in GBM through direct interaction with tumor cells [13]human astrocytes were used as the control system in our evaluation of the AMPS-CD@RZ system. Synchrotron radiation (SR)-based Fourier transform infrared microspectroscopy (FTIR or μFTIR) was employed to examine glioblastoma and healthy astrocyte cells. SR-FTIR has been previously utilised to characterise glioma blood vessels and glioblastoma, identifying biomolecular markers of these tumors [14, 15]. Chemometric analyses, such as Principal Component Analysis (PCA) and Hierarchical Cluster Analysis (HCA), have shown that the brightness of synchrotron light provides a superior signal quality compared to conventional sources, enabling the detection of subtle glioma-specific molecular markers [15]. It has also been applied to detect hypoxia-induced metabolic changes in glioblastoma cell lines and short-term primary cultures derived from patient samples, revealing increased levels of glycogen and lipids [16]. Similar findings have been observed in glioma stem cells, where alterations in cellular membranes, elevated phosphorylated protein levels, and increased glycogen were reported [17]. Using synchrotron light as an infrared (IR) source, we analysed bio-macromolecular signatures of individual living cells in situ. Infrared spectroscopy offers highly specific molecular information by probing vibrational transitions characteristic of distinct classes of biomolecules [18]. The μFTIR technique enabled the detection of metabolic changes induced by treatment with AMPS-CDs@ RZ nanoparticle treatment in intact living cells. In this study, we evaluated the effects of AMPS-CDs NP as a potential nanotherapeutic agent for RZ and its effect on biomolecular profiles in a patient-derived glioblastoma cell line and non-cancerous astrocyte controls using SR-μFTIR on live cells. We investigated biochemical signatures in cells treated with riluzole alone, AMPS-CDs alone, and the AMPS-CDs@ RZ combination, comparing them to untreated controls. Statistical methods, including PCA and t-distributed stochastic neighbour embedding method (t-SNE) analysis, were used to analyse the data. To the best of our knowledge, this is the first study to apply μFTIR spectroscopy to analyse live GBM cells treated with AMPS-CDs and RZ simultaneously. The synchrotron-based IR source allowed us to assess bio-macromolecular signatures of single cells in situ, enabling the discrimination of the metabolic changes in patient-derived GBM alive cells compared to astrocytes. SR-μFTIR spectroscopy provides a vigorous approach to detecting specific metabolic alterations induced by the AMPS-CDs@RZ nanotherapeutic agent. Statistical analysis further facilitated the interpretation of spectral variability among cells, highlighting fine molecular differences caused by the treatment of brain tumor cells.

In parallel, cryo-soft X-ray tomography (SXT) was employed to observe structural changes in situ in cells treated with AMPS-CDs@RZ. SXT is an imperative technique that enables the imaging of intact cellular structures in their natural state without sectioning or staining, standing out from cryo-electron tomography, with a resolution of 25–40 nm. We used SXT to investigate organelle localisation and ultrastructural changes in GBM and astrocytes after NPs treatments.

This study revealed significant changes in biomolecular profiles following treatment with the nanotherapeutic agent of carbon dots and riluzole, suggesting a tumor-specific mechanism of action. These findings provide

novel insights into the biomolecular changes induced in cancer cells and offer an appealing avenue for understanding the therapeutic potential of AMPS-CDs@RZ in glioblastoma treatment.

Experimental

Preparation of glioblastoma and astrocyte cell samples in culture

This study utilised the glioblastoma cell Line 11ST, derived from a patient and cultured exclusively for these experiments. The cell line was originally cultivated at the University of Medicine in Göttingen, Germany, cryopreserved and transported to the ALBA facility in a cryocontainer. It was rigorously grown for the experiments at the ALBA Biology Laboratory. Ethical approval for this study was unwaveringly obtained from the Ethics Committee of the esteemed University Medical Center Göttingen (approval number 11/8/13). Primary cells isolated from the patient were cultured in complete medium comprising MEM (500 mL, Gibco), 10% heat-inactivated fetal calf serum (Gibco), 2 mM L-Glutamine (Gibco), 1 mM sodium-Pyruvate (Gibco, 11360-039), and PenStrep (Thermo Fisher).

Cells were seeded at a density of 4×10^4 cells per 25 cm [2] flask with 5 mL of complete medium and incubated at 37 °C with 5%CO_2. Prior to data collection, cells were briefly rinsed with Ca^{++}/Mg^{++}-free Dulbecco's phosphate-buffered saline (D-PBS) and trypsinised. They were then seeded onto 0.5 mm-thick CaF_2 glass coverslips and cultured in complete medium for 24 h. Subsequently, they were treated with 50 μM of riluzole, 0.1 mg mL-1 *AMPS-CDs* nanoparticles, or a combination (AMPS-CDs@RZ) for an additional 24 h. Untreated cells served as controls. Concentrations were optimised to avoid precipitation and ensure cell viability. Cell morphology was inspected to exclude non-viable cells (rounded morphology) before Fourier-transform infrared (FTIR) analysis. Live-cell devices were assembled, and spectra were collected within 2 h while maintaining cells at 37 °C. Complete profiling of organic compounds at the single-cell level in each case was evaluated.

AMPS-based carbon nanoparticles (AMPS-CDs) with a size of ~ 5 nm was synthesised using the method described previously [7]. Briefly, AMPS (Sigma-Aldrich. Barcelona, Spain) underwent hydrothermal processing at 200 °C for 4 h, in the presence of trifluoracetic acid. The cooled product was filtered to remove carbonised material, lyophilised to yield a bright white powder, and labelled as *AMPS-CDs* NPs.

Human astrocytes, isolated from healthy cerebral cortex tissue, were purchased from Innoprot (Derio, Bilbao, Spain (# P10251) and were cultured in complete astrocyte medium containing high-glucose DMEM (GIBCO), 10% fetal bovine serum (GIBCO), 100 UmL^{-1} penicillin-streptomycin (GIBCO), 2 mM L-Glutamine (GIBCO), 1×non-essential amino acids (GIBCO) and 1×N2 supplement (GIBCO). Astrocytes were prepared and treated under the same conditions as glioblastoma cells, and FTIR measurements were conducted as described.

Cell viability assay

Cellular metabolic activity was evaluated using the MTT assay as an indirect mark of cell viability that will be the term used in the text onwards. Cells were seeded at a density of 1×10^4 cells per well in 96-well plates with 200 μL of medium per a well, and incubated at 37 °C with 5% CO_2 for 24 h (5 replicates per condition). After replacing the medium with 200 μL fresh medium containing 0.5 mg/mL 3-[4,5-dimethylthiazol-2-yl]−2,5-diphenyl tetrazolium bromide (MTT), cells were incubated for an additional 2 h. The medium was then removed, and formazan crystals were solubilized by adding 200 μL of DMSO and thoroughly mixing the solution to dissolve the dye. Absorbance at 550 nm was measured using a microplate reader (Dynatech MR7000).

Relative cell viability (%) was calculated based on the absorbance readings, with error values derived from the following equations. Negative control wells contained cell culture medium without nanoparticles nor riluzole, and positive control wells included Triton X-100 to induce complete cell lysis:

$$RCV(\%) = (([Abs]_{test} - [Abs]_{Pos.Ctrl})/([Abs]_{Neg.\ Ctrl} - [Abs]_{Pos.\ Ctrl})) \times 100.$$

$$Error\ (\%) = RCV_{test} \times SQRT\ [(\sigma_{test}/[Abs]_{test})^2 + (\sigma_{test}/[Abs]_{test})^2]$$

where σ is the standard deviation.

Synchrotron radiation-based (SR)-FTIR measurements

SR-FTIR measurements were conducted using the 3000 Hyperion microscope coupled to a Vertex 70v spectrometer, equipped with a liquid N_2-cooled mercury cadmium telluride (MCT) detector, at the MIRAS beamline of the ALBA Synchrotron in Barcelona, Spain. Spectra were collected in transmission mode with a 36× Schwarzschild objective and 10 μm × 10 μm aperture. A total of 44 to 105 spectra per treatment were systematically recorded in the mid-infrared range of 4000–900 cm^{-1}, with a spectral resolution of 4 cm^{-1} averaging 256 scans per spectrum.

The live-cell device, once assembled with the cells and medium, was carefully maintained at 37 °C throughout the measurements. Spectra were collected under precise conditions, with the sample monitored using the VIS microscope. A maximum of 2 h was allowed for data acquisition. For every ten proximal cells measured, a buffer point spectrum was acquired under identical acquisition parameters to facilitate subsequent water

subtraction. The background spectrum was recorded at the beginning of each measurement session using a 0.5 mm-thick CaF_2 substrate. Synchrotron radiation served as the infrared light source, and data acquisition was controlled using the OPUS 8.0 software package (Bruker, Germany).

Rigorous spectral analysis was performed, which included water subtraction for each individual cell, followed by a second derivative transformation (3rd polynomial order, 29 smoothing points, and vector normalisation). Principal Component Analysis (PCA) was then applied to each dataset after water subtraction, second derivative calculation, and spectral normalisation. t-SNE analysis was also conducted to further interpret the data. Both PCA and t-SNE analyses were carried out using the Quasar software (Bioinformatics Laboratory, University of Ljubljana, v. 1.7.0) [19, 20].

Water Subtraction procedure

Water contribution in live-cell spectra was subtracted using a script previously developed by Vaccari and colleagues [21]along with a modified version created at the ALBA Synchrotron. Briefly, the water signal from the medium surrounding the cells was subtracted from each spectrum using a subtraction factor that ranged from 0.8 to 0.95 for each individual cell. This process was facilitated by a graphical user interface (GUI) developed using the Taurus software [22]with the subtraction factor adjusted based on the Amide I and Amide II peak height ratio of 1:0.6 (± 0.1).

The Amide I/II ratio of 1:0.6 (± 0.1) was determined by measuring the peak heights for both Amide I and Amide II in the dry cell spectra. Using this ratio, the GUI was applied to fine-tune the water subtraction factor by visualizing the spectra and ensuring the Amide I/II ratio was maintained for each cell. The developed GUI optimizes both the Amide I/II peak ratio and the water subtraction procedure, which was applied to spectra acquired in the SR-FTIR transmission configuration.

Synchrotron radiation-based soft X-ray tomography (SXT)

GBM and astrocyte cells were cultured on gold grids coated with carbon mesh foil (R2/2), which had been glow-discharged for electron microscopy. The cells were then treated with riluzole and carbon dots for 24 h. Following treatment, the samples were blotted for 3 s and vitrified in liquid ethane using an EM GP vitrification unit (Leica Microsystems, Wetzlar, Germany). Vitrified samples were subsequently transferred to the cryo-stage of a full-field transmission X-ray tomography microscope maintained at liquid nitrogen temperature.

Tomograms of the vitrified samples were recorded at the Mistral beamline of the ALBA Light Source (Spain), using soft X-rays with an energy of 520 eV [23]. Imaging was performed with a zone plate objective that has an outermost zone width of 40 nm. Since zone plate objectives use diffraction rather than refraction to focus X-rays, the resolution is limited to about 40 nm. Tilt series were collected with 1° increments over typically a ± 70° angular range, with a single image acquisition time of 1 s. The tilt series were aligned using cross-correlation, and reconstruction was carried out with the iterative SIRT method in TOMO3D. Manual segmentation of the tomograms was performed by tracing membranous structures with the Amira segmentation software (FEI Visualization Sciences Group).

Quantification and statistical analysis

Statistical analyses for the MTT test were performed in GraphPad Prism 7 using Student's t-test. Significance is indicated in each figure legend $^{*}p < 0.05$; $^{**}p < 0.01$. The data are presented as the mean ± SD.

For the FTIR analysis, the area under peaks was calculated and statistical tests were performed using the One-way ANOVA *Tukey* test in OriginPro 9.1 software (Northampton, MA, USA). Differences were considered significant with $^{*}p < 0.05$, $^{**}p < 0.01$, $^{***}p < 0.001$.

Results

AMPS-CDs and riluzole drug (AMPS-CDs@RZ) as a nanotherapeutic agent: cytotoxic effects on glioblastoma and astrocyte cells

To investigate the potential effects of riluzole (RZ), both alone and in combination with the AMPS-CDs nanoparticle (NP), we first assessed the cytotoxicity of various concentrations of NPs and riluzole on primary glioblastoma 11ST cells and healthy non-tumor human astrocytes (Fig. 1A, B, respectively). Notably, AMPS-CDs NPs, at relatively high concentrations, were found to slightly enhance cell viability without inducing harmful effects on either cell type (Fig. 1, "No RZ" group).

To determine the optimal concentrations of AMPS-CDs NPs and riluzole, we tested a range of concentrations: AMPS-CDs from 0.01 to 1 mg/mL and riluzole from 5 to 500 µM. For glioblastoma multiforme (GBM) cell culture experiments, we focused on the lowest concentration of riluzole near its IC50, corresponding to doses that induce approximately 50% cell death. IC50 values are widely used to estimate a substance's efficacy [24]. Previous studies indicated that 50 µM riluzole approximates the IC50 for GBM cells, demonstrating significant molecular and survival effects on these cells [14, 25].

Our results showed that combining 50 µM riluzole with 0.1 mg/mL AMPS-CDs significantly reduced GBM cell viability (%RCV) from 62.7 ± 2.4% to 55.2 ± 3.1%. This combination mimicked the cell death effect observed with 100 µM riluzole, which resulted in 52.3 ± 1.7% RCV (red arrow in Fig. 1A). Interestingly, increasing the

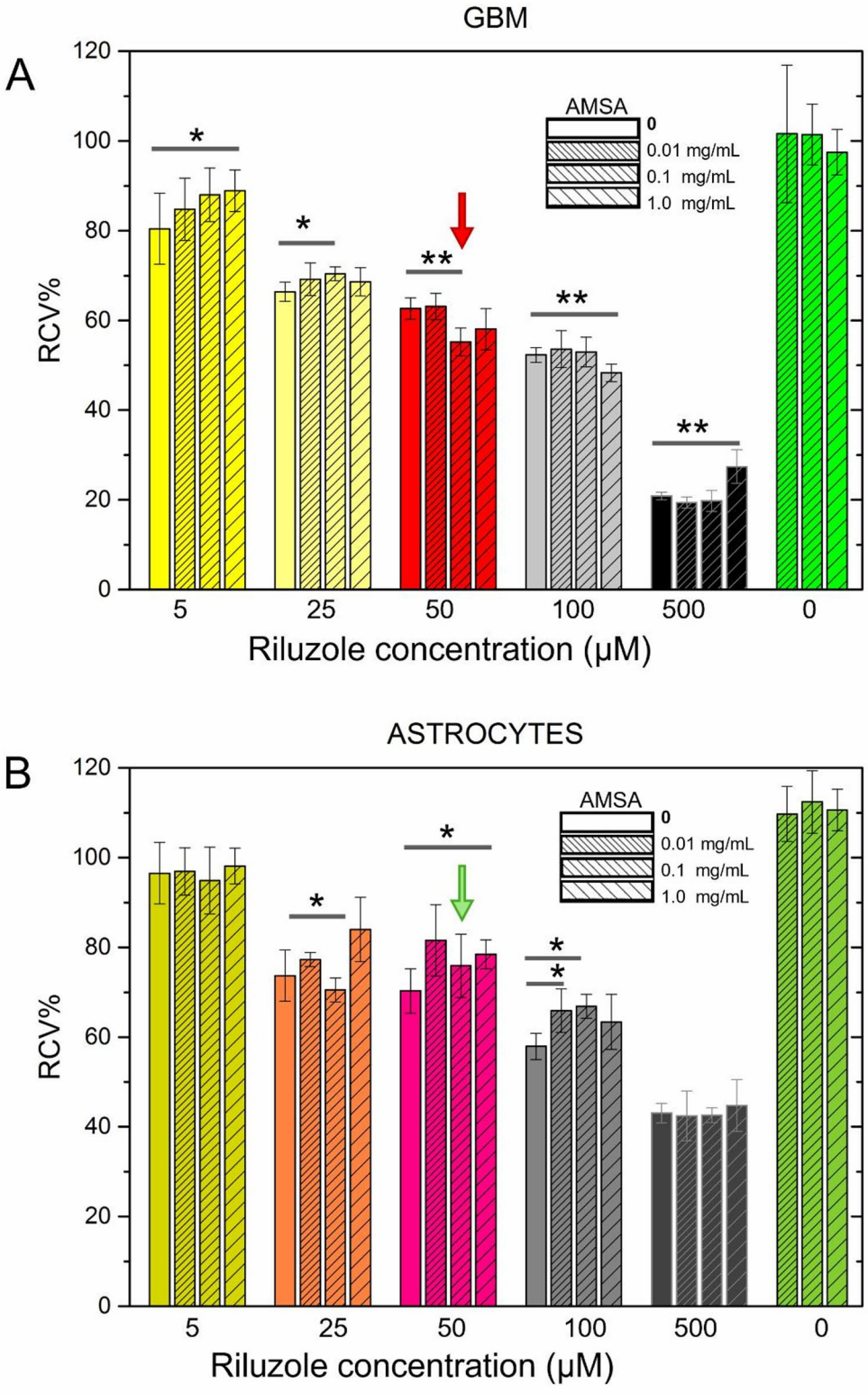

Fig. 1 Relative cell viability ± SD after treatment with different concentrations of riluzole (RZ), carbon dots AMPS-CDs NPs (No RZ group) and carbon dots and riluzole (AMPS-CDs@RZ) on GBM 11ST cell line (**A**) and human astrocyte cell line P10251 (**B**). Red and green arrows indicate the chosen concentration of riluzole and carbon dots. Student's t-test p-value indicating significant differences when compared with cells treated with RZ solely are shown (* $p < 0{,}05$, ** $p < 0.01$). The red and green arrows point to selected riluzole and AMPS-CDs concentration for further analysis

AMPS-CD concentration to 1 mg/mL alongside 50 μM riluzole improved cell viability to 58.1 ± 4.6%, suggesting a potential protective effect of higher AMPS-CD concentrations on GBM cells.

In parallel, we evaluated these concentrations in the astrocyte cell line (green arrow in Fig. 1B). Riluzole had a significantly reduced effect on astrocyte cell death at all tested concentrations, indicating a more pronounced cytotoxic effect on rapidly proliferating tumor cells than on non-tumor astrocytes (Figure S1). This trend was consistent when combining 50 μM riluzole with different AMPS-CD concentrations on astrocytes (Figure S1).

Remarkably, combining 50 μM riluzole with 0.1 mg/mL AMPS-CDs increased astrocyte cell viability (%RCV = 76 ± 7%), contrasting with the decreased viability observed in GBM cells (Fig. 1A and B). This indicates that the riluzole and AMPS-CDs combination may selectively enhance GBM cell death while promoting survival in non-tumor astrocytes.

Based on these findings, we selected the combination of riluzole (50 μM) and AMPS-CDs (0.1 mg/mL) for further analysis to explore its effects on biomacromolecular in both GBM and non-tumor astrocyte cells.

In previous studies, this GBM cell line was analysed using synchrotron light-based X-ray microscopy techniques [26]providing elemental and structural imaging of the cells. Here, we investigated the effects of AMPS-CDs@RZ treatment on key bio-macromolecules in both GBM and healthy astrocytes using synchrotron-based live cell Fourier-transform infrared (FTIR) spectroscopy. Additionally, we assessed subcellular structural changes using soft X-ray tomography (SXT) to examine treatment-induced morphological changes.

Live cell μFTIR analysis of GBM and astrocytes treated with AMPS-CDs and riluzole (AMPS-CDs@RZ)

We further analysed the effect of novel carbon dots and riluzole as a potential nanotherapeutic agent in cells. The AMPS-CDs were previously characterised in detail, and initial assays confirmed the efficacy of AMPS-CDs@RZ on the GBM cell line [7]. In this study, we focused on a comparative analysis of GBM and human astrocyte cell line, serving as non-cancerous control cells, to thoroughly investigate changes in key biomacromolecules, including lipids, proteins, esters, carbohydrates, and nucleic acids.

Fingerprint area

Figure 2 provides detailed spectra of the main biomacromolecules in the fingerprint region (1800–900 cm^{-1}) of GBM 11ST and astrocyte cell lines AMPS-CDs@RZ treatment under live conditions.

Following water correction, baseline correction, and vector normalisation of individual cell spectra (N = 18–105), we used average spectra to compare key spectral bands corresponding to esters, proteins, cholesterol, carbohydrates, and nucleic acids (Fig. 2). The t-distributed Stochastic Neighbour Embedding (t-SNE) analysis of single-cell IR signatures revealed distinct group separations, more pronounced in GBM cells than astrocytes Figs. 2B, F, and SFig.2. This separation was confirmed with PCA scatter plots (Figs. 2 D, G). PCA loading plots for GBM and astrocytes (Figs. 2 C and H), indicated that separation along PC1 was primarily due to differences in protein structure and DNA between the two cell types. PC3 loadings showed maximum contributions from carbonyl groups (mainly lipids: this band will be evaluated further in the text) and minimum from the Amide I region in GMB RZ-treated cells, while astrocytes exhibited opposite trends—minimum for esters and maximum for proteins, as indicated by arrows in the scatter plots (Figs. 2D, G). Given that protein bands were the primary drivers of differences across PCs, Amide I and Amide II bands were deconvoluted and analysed in detail (Figs. 3 and 4).

Amide regions analysis

FTIR spectra of Amide I and Amide II regions in GBM cells are shown in Fig. 3. Following the deconvolution of the two main protein peaks, the areas under sub-peaks corresponding to secondary structures were analysed and displayed in box plots.

Key peaks included 1655 cm^{-1} (α-helix), 1635 cm^{-1}(β-sheet), 1610 cm^{-1} (free amino acids side-chains), 1572 cm^{-1}(glutamine), 1545 cm^{-1} (α-helix in Amide II) and 1515 cm^{-1} (tyrosine). The assignment of peaks was done using previously described spectral components associated with different secondary structures [27, 28]. Significant differences were observed in the Amide I region at ~1682, ~1655, ~1635, and ~1610 cm^{-1}, representing changes in turn and loops, α-helix and β-sheet structure, and side chains conformations respectively (as assigned in Fig. 3). In the Amide II area, the most pronounced changes were at 1572 cm^{-1} (glutamine) and 1545 cm^{-1} (α-helix), followed by peaks at 1655 cm^{-1} and 1635 cm^{-1} in the Amide I region. Both treatments, AMPS-CDs@RZ and RZ, reduced β-sheet and α-helix structures, with a more marked effect from AMPS-CDs@RZ. The area of peaks associated with two amino acids, glutamine and tyrosine, was also analysed and showed significant differences.

Astrocyte protein conformations were analysed similarly (Fig. 4). AMPS-CDs@RZ increased β-sheet structures compared to RZ alone, returning to control levels. Conversely, α-helix levels in Amide II decreased significantly in AMPS-CDs@RZ-treated astrocytes. Interestingly, deconvoluted the Amide I peak showed AMPS-CDs@RZ and AMPS alone resulted in the highest

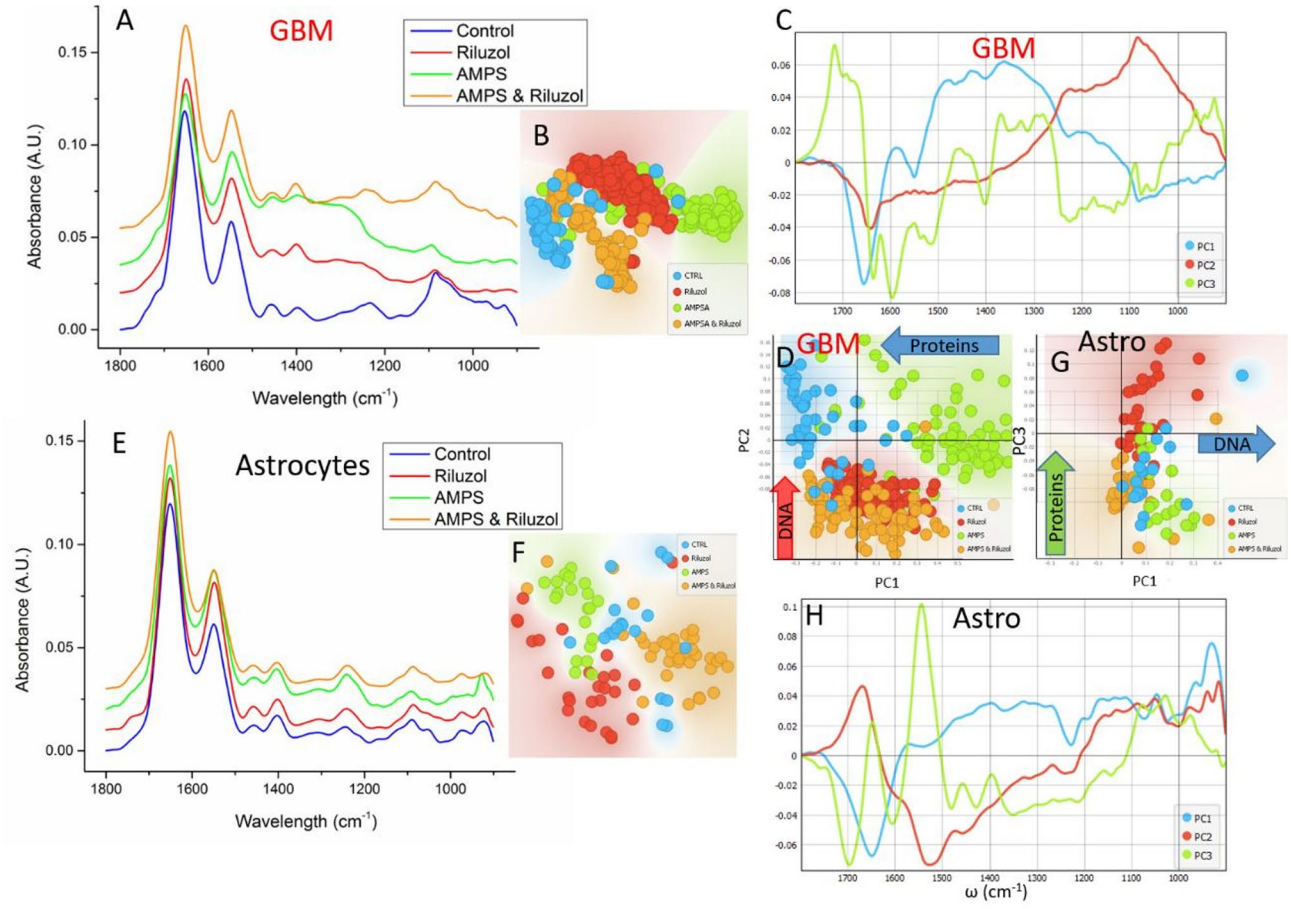

Fig. 2 The FTIR averaged spectra of live cells 11ST GBM cells (**A**) and human astrocytes (**E**) grown in cell medium (blue), after treatment with RZ (red), after treatment with AMPS-CDs NPs (green) and AMPS-CDs@RZ (orange) in the spectral region of the fingerprint 900–1800 cm − 1. The t-SNE analysis of GBM (B) and astrocytes (F). PCA scatter plot of PC1 and PC3 for GBM (**D**) and astrocytes (**G**). The PCAs (loading values) of the first three principal components, PC1 (blue), PC2 (red) and PC3 (green) of GBM (C) and astrocytes (**H**) show the contribution of individual absorbance. *N* = 18–105

α-helix peak areas in the Amide I region, suggesting that AMPS-CDs stabilise α-helices in non-tumor cells while exerting contrasting effects on GBM cells. Significant effects were also observed in amino acids (1610 cm^{-1}), Tyr (1515 cm^{-1}), and Gln (1572 cm^{-1}); however, these effects were less pronounced than in GBM cells. Notably, glutamate levels increased significantly in GBM after AMPS-CDs@RZ treatment but decreased in astrocytes, further highlighting differential responses between tumor and non-tumor cells.

The PCA analyses confirm these findings (in supplemental material Figures S4, S5).

Glutamate, a central excitatory neurotransmitter synthesised in the central nervous system from glutamine *via* the glutamate-glutamine cycle, plays a dual role in supporting neuronal communication and acting as a precursor for GABA synthesis [29]. However, elevated glutamate concentrations can lead to cell death through necrosis or apoptosis in cultures of neurons or cerebellar granule cells [30]. This highlights the importance of regulating glutamate levels for proper neural cell behaviour, underscoring the potential of FTIR spectroscopy to detect glutamate as a target for AMPS-CDs@RZ treatment.

Lipid analysis

Comparative analysis of lipid regions across all cell cultures revealed distinct responses to *AMPS-CDs* as shown in Figs. 5a and 6a. t-SNE analysis highlighted the segregation of GBM cells after RZ treatment and astrocytes after AMPS-CDs@RZ treatment (Fig. 5B).

PCA analysis indicated significant separation along PC1 following AMPS-CDs@RZ treatment, and along PC2 following riluzole treatment, in GBM cells (Fig. 5D).

In GBM cells, PC1 primarily reflected changes in asymmetric and symmetric CH_2 stretching bands (2922 and 2855 cm^{-1}), which were most pronounced following AMPS treatment (Fig. 5C). PC2 indicated a decrease in the asymmetric CH_2 band (2922 cm^{-1}) after riluzole

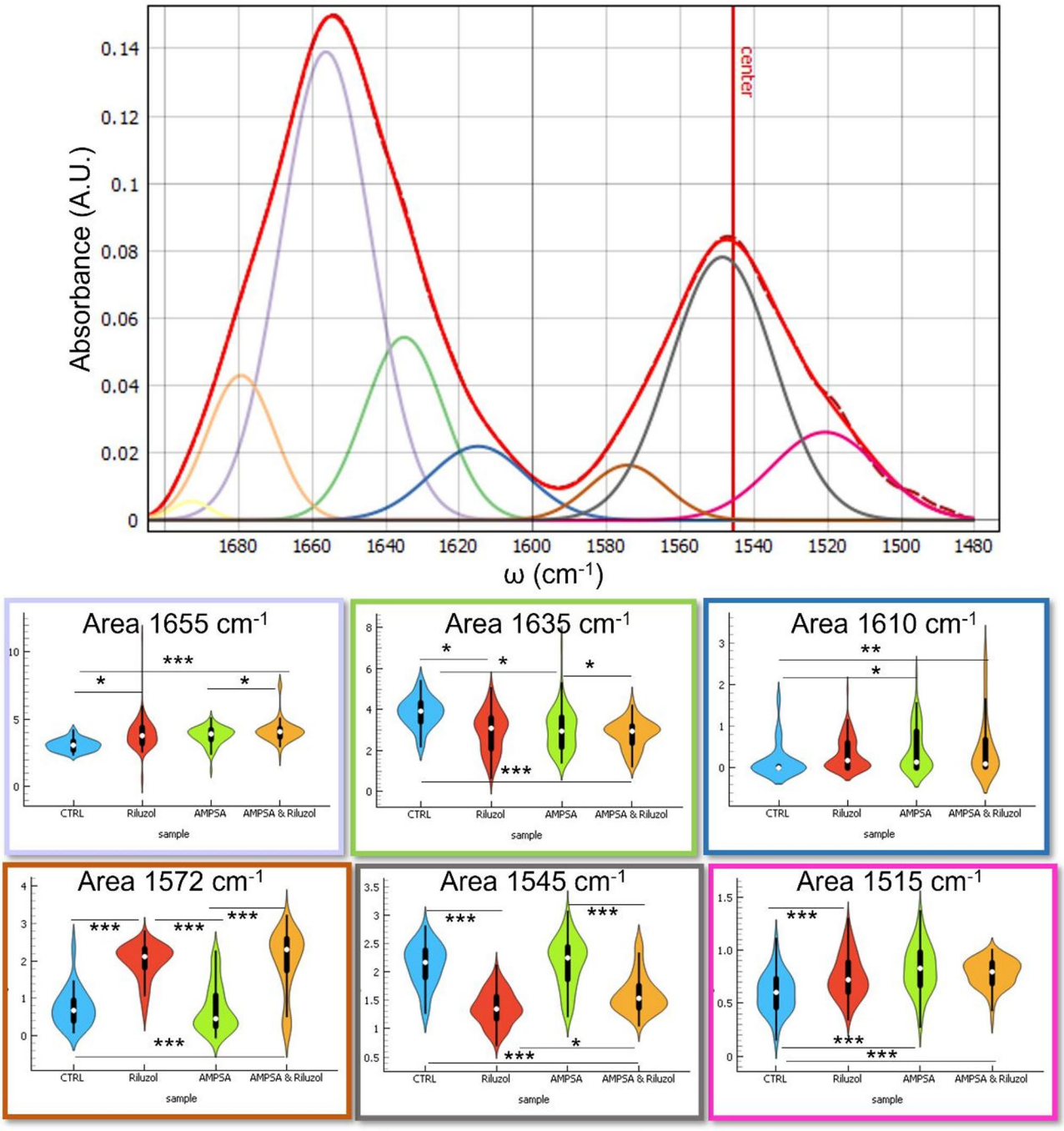

Fig. 3 FTIR averaged and deconvoluted spectra Amide I of the 1480–1710 cm^{-1} area of the 11ST GBM cell line. The baseline-corrected and vector-normalised spectra of live cells are shown. Integrated area of α-helix proteins with a maximum at 1655 cm^{-1}, the β-sheet parallel conformation bands with a maximum at 1635 cm^{-1}, side chains of amino acids (maximum at 1610 cm^{-1}), free amino acids side-chains as glutamine at 1572 cm^{-1}, Tyrosine 1515 cm^{-1} and α-helix in Amide II at 1545 cm^{-1}. *$p < 0.05$, **$p < 0.01$, ***$p < 0.001$ annotate the significant difference between groups. $N = 44–105$

treatment, while symmetric CH_2 groups (2855 cm^{-1}) increased in AMPS and control conditions.

Analysis of lipid-associated peaks—including the carbonyl group band (~1740 cm^{-1}), CH_2/CH_3 band ratios, and C = O vs. CH_2 and CH_2 bands—revealed a significant decrease in carbonyl groups after AMPS-CDs@RZ treatment in GBM cells compared to controls (Fig. 5 E-G). These carbonyl groups, originating from lipid ester bonds, represent fatty acid and glycerol components of lipids. The CH_2/CH_3 ratio—a reliable indicator of lipid saturation [31, 32]decreased after AMPS treatment (Fig. 5E). A higher CH_2/CH_3 ratio indicates increased

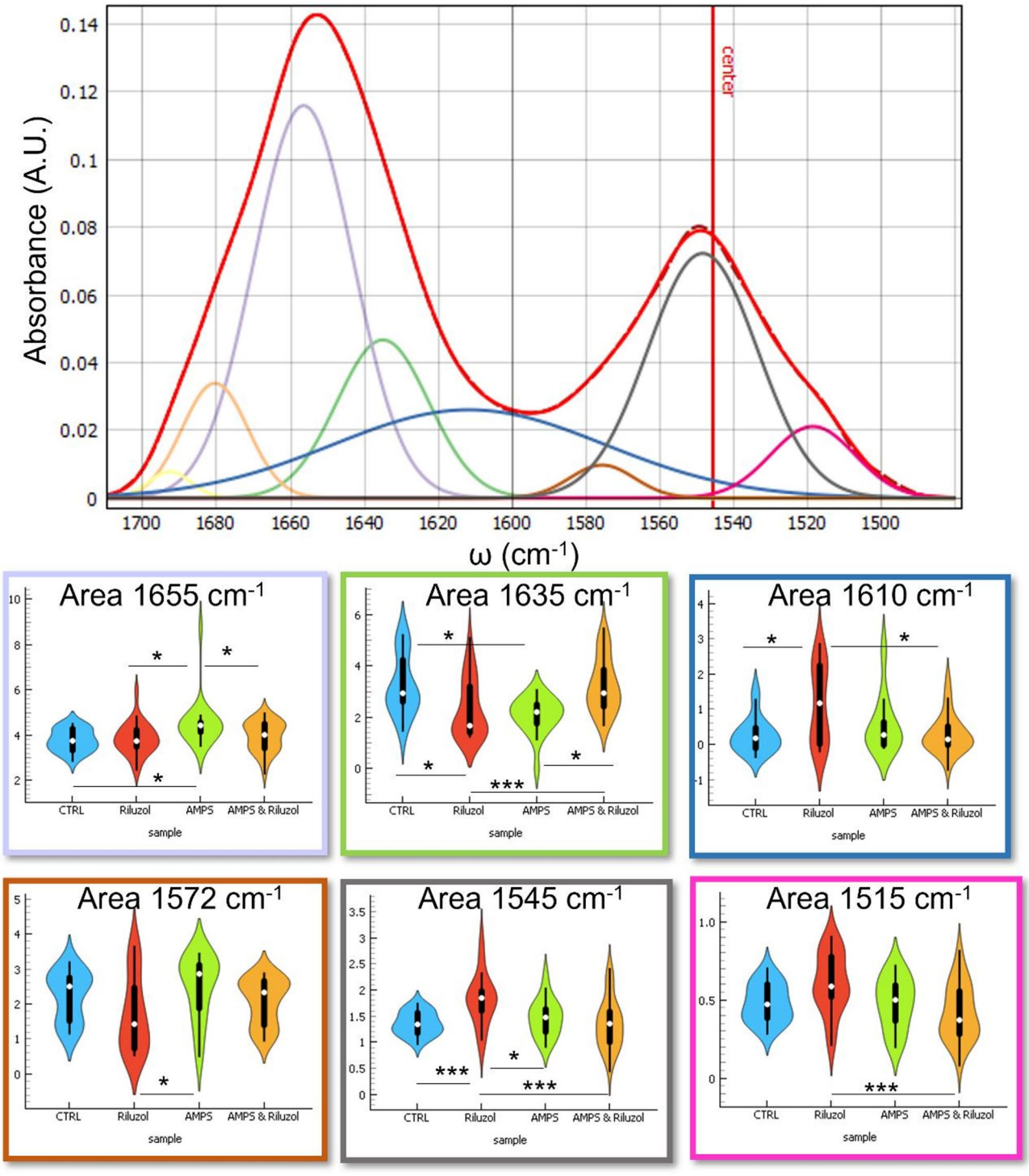

Fig. 4 FTIR averaged and deconvoluted spectra Amide I of the 1580–1710 cm^{-1} area of the astrocyte cell line. The baseline-corrected and vector-normalised spectra of live cells are shown. Integrated area of the α-helix proteins with a maximum at 1655 cm^{-1}, the β-sheet parallel conformation bands with a maximum at 1635 cm^{-1}, side chains of amino acids (maximum at 1610 cm^{-1}), free amino acids side-chains as glutamine at 1572 cm-1, Tyrosine 1515 cm^{-1} and α-helix in Amide II at 1545 cm^{-1}. *$p < 0.05$, ***$p < 0.001$ $N = 18–35$

lipid acyl chain unsaturation [26]often associated with lipid peroxidation [33]. To evaluate lipid peroxidation, the carbonyl group absorption was normalised to total lipid content (C = O to CH_2&CH_3 ratio [34]), revealing an increase following riluzole and AMPS-CDs@RZ treatments, confirming the role of riluzole in promoting lipid peroxidation Fig. 5G. The ratios of the IR bands CH_2/CH_3 and C = O to Amide I were shown to be reliable

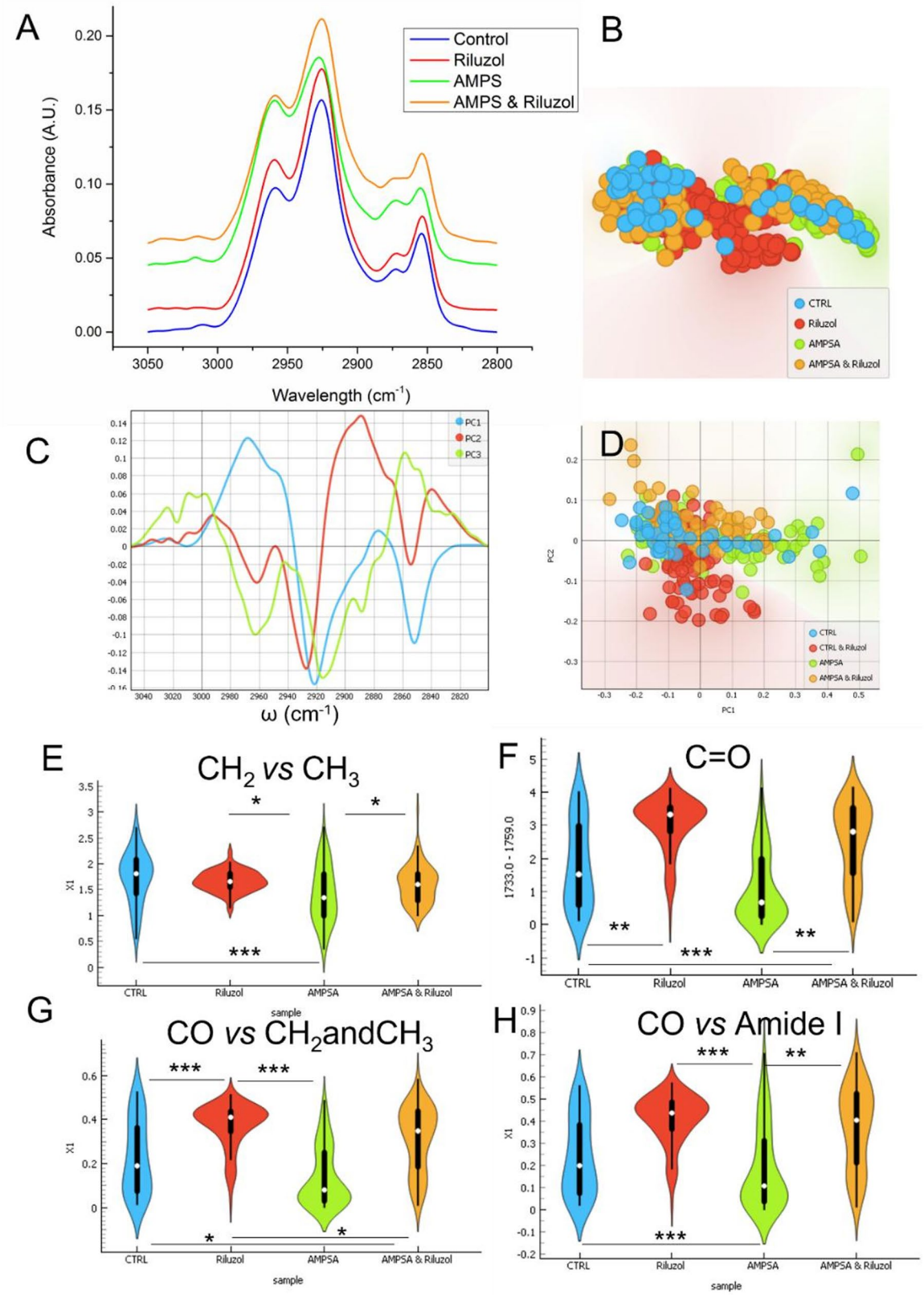

Fig. 5 (See legend on next page.)

(See figure on previous page.)

Fig. 5 (**A**) The FTIR averaged spectra of live cells 11ST GBM cells grown in cells medium (blue), after treatment with riluzole (red), cell culture treated with the AMPS-CDs (green), and cells treated with AMPS-CDs@RZ (orange)in the spectral region of the lipids, 3100–2800 cm^{-1} and the t-SNE analysis of lipids (**B**). The PCA loadings values of the first three principal components, PC1 (blue), PC2 (red), and PC3 (green) (**C**) and PCA scatter plot (**D**). The integrated ratio of asymmetric CH_2 vs. CH_3 bands (**E**), carbonyl groups band (**F**), C = O vs. asymmetric lipids bands (**G**), and C = O vs. Amide I (**H**). *$p < 0.05$, **$p < 0.01$, ***$p < 0.001$, $N = 44–105$

scales of the lipidic character of cells [34]. The ratio C = O to Amide I showed a significant increase after RZ and AMPS-CDs@RZ treatment in GBM cells (Fig. 5H).

In astrocytes, lipid analysis revealed distinct responses to AMPS-CDs@RZ (Fig. 6 A). The t-SNE analysis showed clear segregation for this treatment group (Fig. 6B), while PCA indicated separation along PC1 (AMPS-CDs@RZ and RZ) and PC2 (AMPS-CDs@RZ treatment) (Fig. 6D). PC1 predominantly reflected changes in asymmetric and symmetric CH_2 stretching bands (2922 and 2855 cm^{-1}) observed across all astrocyte treatments (Fig. 6C). PC2 demonstrated an increase in CH_2 bands (2922 and 2855 cm^{-1}) following AMPS-CDs@RZ treatment.

Notably, carbonyl group bands increased after RZ treatment but decreased with AMPS-CDs (Fig. 6E). The CH_2/CH_3 ratio significantly increased following AMPS-CDs@RZ treatment compared to controls, while the C = O vs. CH_2 and CH_3 ratio decreased compared to riluzole-only treatment (Fig. 6F, G). The ratio C = O to Amide I did not show a significant increase after RZ and AMPS-CDs@RZ treatment in comparison to control cells, but only in comparison to AMPS treatment (Fig. 6H).

These results suggest that AMPS-CDs@RZ mitigates riluzole-induced lipid peroxidation specifically in non-tumor astrocytes but not in GBM cells. This effect demonstrates the potential of AMPS-CDs@RZ to selectively target glioblastoma, offering a promising mechanism for improved drug delivery and efficacy.

Structural changes detected by cryo-SXT in intact cells

Cryo-soft X-ray tomography (cryo-SXT) is a powerful microscopy technique that provides detailed inner structural information about intact single cells by utilising energy within the so-called "water window." This method was employed to investigate structural changes in situ in treated and untreated cells.

Figure 7 A illustrates a high-resolution mosaic of partially overlapping soft X-ray images that were seamlessly stitched together to provide a comprehensive overview of an entire GBM cell. The cells displayed a typical stellate morphology with an approximate length of 50 µm. Notably, key cellular components—including the nucleus, nucleolus, nuclear membrane (NM), mitochondria (M), endoplasmic reticulum (ER), vesicles, and the Golgi apparatus (G)—were discernible in the virtual slide presented in Fig. 7B.

Figure 7 C depicts a segmented image that highlights the proximity of mitochondria (red) to the nucleus (green). In addition, in GBM cells treated with AMPS@RZ, nuclear membrane blebbing was observed (light orange arrow, Fig. 7B C). These blebs appeared to be surrounded by numerous mitochondria (red), suggesting possible communication between these organelles. Furthermore, the ER showed a markedly open, reorganised structure, while numerous vesicles (light green) were distributed throughout the cytoplasm. A round dark structure in the tomogram (blue) likely represents a nanoparticle encapsulated with riluzole, potentially interacting with other cellular components.

Our investigation focused on the perinuclear region, where tomograms revealed significant alterations in the nuclear membrane following AMPS-CD@RZ treatment (Fig. 8). Strategically guided by mosaic images, 5–10 tomograms were recorded for each treated cell, targeting this area.

Figure 8 compares SXT images of control cells, riluzole-treated cells, AMPS-CDs@RZ-treated GBM cells, and healthy astrocytes. The most pronounced effects were seen in GBM cells treated with AMPS-CDs@RZ, particularly on the nuclear envelope (yellow arrow). This treatment induced specific intracellular changes, including the formation of nuclear envelope blebbing (orange arrow, Fig. 8). Additionally, an increase in mitochondrial volume and mitochondrial fusion was observed (red arrow). A notable number of intracellular vesicles also formed (black arrow, Fig. 8), with pleomorphic vesicles ranging in size from 90 to 800 nm and exhibiting dark or light lumens after AMPS-CDs@RZ treatment.

Along with these nuclear changes, lipid membrane reorganisation of the ER was markedly enhanced following AMPS-CDs@RZ treatment. In contrast, riluzole treatment caused minimal subcellular alterations. Although a few dark vesicles were present around the nucleus, the nuclear membrane (NM) remained unaffected. Astrocytes exhibited fewer changes after treatment, with lipid droplets observed in all conditions., Lipid droplets, which are normal components of cellular metabolism, store neutral lipids as triacylglycerols and cholesterol esters. This can be mobilised as an energy source during metabolic stress or when energy demands exceed immediate cellular resources. While AMPS-CDs@RZ treatment induced dramatic changes in GBM cells, the impact on astrocytes was comparatively limited, underscoring the selective effects of this treatment.

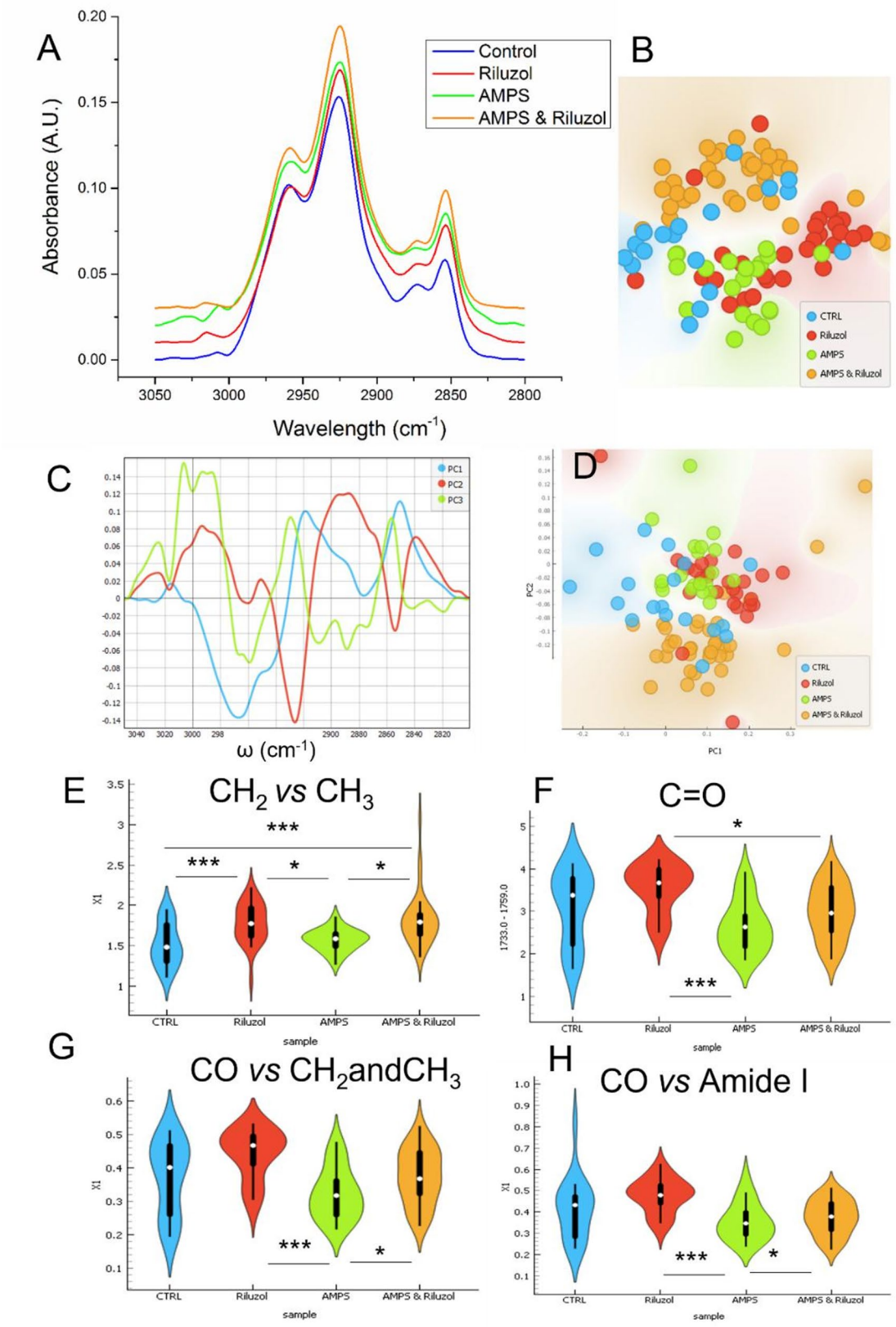

Fig. 6 (See legend on next page.)

(See figure on previous page.)

Fig. 6 (**A**) The FTIR averaged spectra of live human astrocyte cell line grown in cells medium (blue), after treatment of riluzole (red), human astrocyte cell culture treated with the AMPS-CDs (green), and astrocyte treated with AMPS-CDs@RZ (orange) in the spectral region of the lipids, 3100–2800 cm^{-1} and the t-SNE analysis (**B**). The PCA loadings values of the first three principal components, PC1 (blue), PC2 (red) and PC3 (green) (**C**) and PCA scatter plot (**D**). The integrated ratio of asymmetric CH_2 vs. CH_3 bands (**E**), carbonyl groups band (**F**), C = O vs. asymmetric lipids bands (**G**), and C = O vs. Amide I (**H**) $^*p < 0.05$, $^{***}p < 0.001$. $N = 18–35$

Discussion

Riluzole, a benzothiazole derivative, is known to inhibit the proliferation of diverse cancer cell types, including skin, breast, pancreas, colon, liver, bone, lung, nasopharynx, and brain [9, 35, 36] and it is also effective with GBM cell lines [14, 25, 37, 38]. Riluzole disrupts multiple cellular mechanisms such as glutamate secretion, growth signalling pathways, calcium homeostasis, glutathione synthesis, and DNA integrity, while also influencing autophagy and apoptosis pathways [36]. Intriguingly, while cancer cells expressing glutamate receptors often respond to riluzole, some cancer cells lacking these receptors also exhibit sensitivity to the drug [36].

Glutamate, the principal excitatory neurotransmitter in the mammalian brain, functions *via* two receptor classes: ionotropic glutamate receptors (iGluRs) and metabotropic glutamate receptors (mGluRs) [39]. iGluRs regulate ion intake, while mGluRs, as G protein-coupled receptors (GPCRs), mediate stress responses and cellular survival. Despite their diversity, both receptor types share structural similarities, including transmembrane α-helices [40]. The cystine-glutamate antiporter (xCT), composed of 12 transmembrane helices [41]regulates intracellular antioxidant systems and plays a critical role in cancer growth and invasion [42]. Excessive glutamate secretion by glioma causes neurotoxicity, facilitating tumor progression [43]. Riluzole mitigates this effect by downregulating xCT, reducing glutamate secretion, and impairing cancer cell survival [36, 44].

The transmembrane regions of many integral membrane proteins, primarily formed by α-helices, undergo conformational changes during functional activation [45]. We may speculate that these structural rearrangements underlie riluzole effects on α-helix-enriched proteins within the glutamate pathway, as previously suggested [46]. Such mechanisms highlight the potential of advanced imaging and spectroscopy tools to investigate molecular alterations induced by riluzole under physiological conditions.

In earlier work, we demonstrated that GBM cells from different patients exhibit distinct cytoskeletal and elemental profiles under cryogenic conditions [26]. Using Fourier-transform infrared spectroscopy (FTIR), we also identified specific bio-macromolecular changes in GBM cells following riluzole treatment [14]. Building on these findings, we employed multifunctionalized carbon dots (AMPS-CDs) as nano-deliveries for riluzole, demonstrating their ability to enhance drug efficacy in GBM cells [7].

Our study reveals several advantages of using AMPS-CDs to deliver riluzole: (*i*) improved cytotoxicity against GBM cells, (*ii*) reduced drug concentration requirements to be effective, and (*iii*) minimised adverse effects on healthy astrocytes. Nano-deliveries are an advanced approach to drug delivery, offering a promising solution to overcome challenges associated with conventional drug delivery systems. By targeting glioblastoma cells specifically, nano-deliveries like AMPS-CDs reduce off-target effects, enhance therapeutic precision, and mitigate systemic side effects.

Lipid peroxidation and oxidative stress

One of the most prominent outcomes of AMPS-CDs@RZ treatment was its effect on lipid peroxidation. This treatment increased lipid peroxidation in GBM cells, as evidenced by the higher ratio of C = O absorbance relative to CH_2 and CH_3 asymmetric bands. Conversely, in healthy astrocytes, the treatment normalised lipid peroxidation levels. Excessive lipid oxidation disrupts membrane integrity, modifies proteins and nucleic acids, and may culminate in cell death [47]. While the mechanism of riluzole on cell death is not fully understood, recent studies show that RZ inhibits glutathione levels and elevates reactive oxygen species in pancreatic tumour cells [48]. Although multiple oxidant compounds, such as hydrogen peroxide, are widely recognised as mediators and inducers of oxidative stress, increasing attention is being paid to the role of lipid hydroperoxides as critical mediators of cell death. Lipid peroxides have long been appreciated as critical for the progression and regulation of inflammation [49, 50]. Lipid hydroperoxides are pivotal in inflammation and cell death pathways, particularly in the brain, where high oxygen levels and free fatty acid metabolism create an environment conducive to peroxidation [51]. Interestingly, AMPS-CDs alone reduced lipid peroxidation in astrocytes, indicating their potential utility in mitigating oxidative stress modulators in diseases characterized by excessive ROS production as neurogenerative diseases [52].

Our results may provide a therapeutic alternative to current chemotherapeutic options for cancers that have evolved mechanisms to evade apoptotic signals, induction of lipid peroxidation and ferroptosis.

Structural insights from soft X-ray tomography

Soft X-ray tomography (SXT) provided valuable insights into cellular alterations following AMPS-CDs@RZ

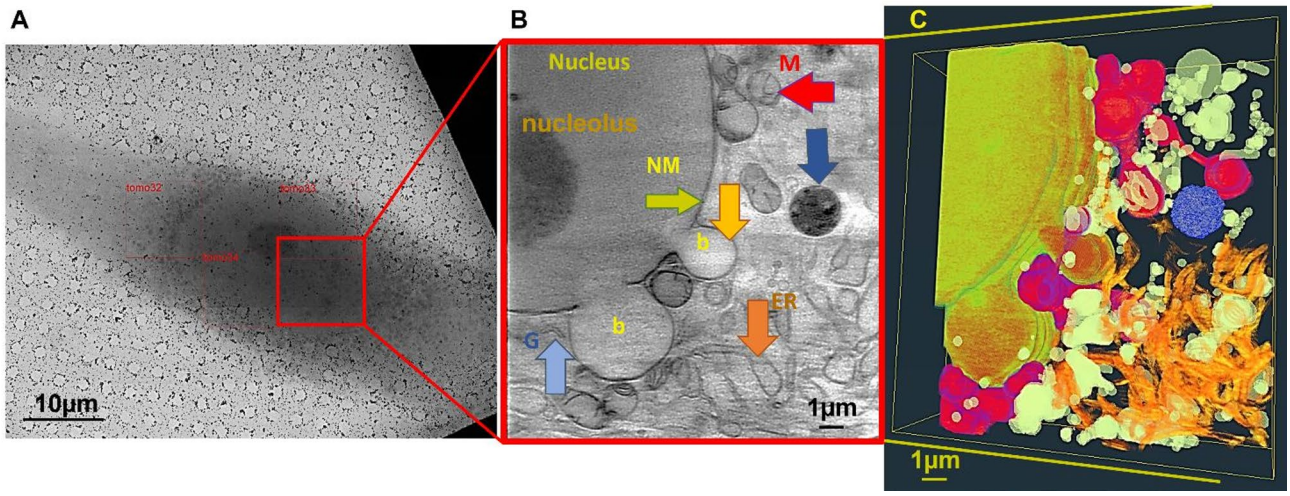

Fig. 7 Soft X-ray tomography overview of AMPS@RZ treated GBM cells after 24 h: cryo-visible light microscopy of a vitrified single cell on carbon foil (**A**). The red square represents a field of view of one tomogram. A typical virtual slice of a tomogram is shown in **B**. Organelles as the nucleus and nucleolus, are marked. The red arrow represents mitochondria (M), the blue one the vesicle, the orange one represents the endoplasmic reticulum (ER), and the light blue arrow points to the Golgi apparatus (G). The nuclear membrane is shown, and the yellow arrow points out the nuclear envelope blebbing (b) in GBM cells. The segmented tomogram (**C**), with organelles color as described previously

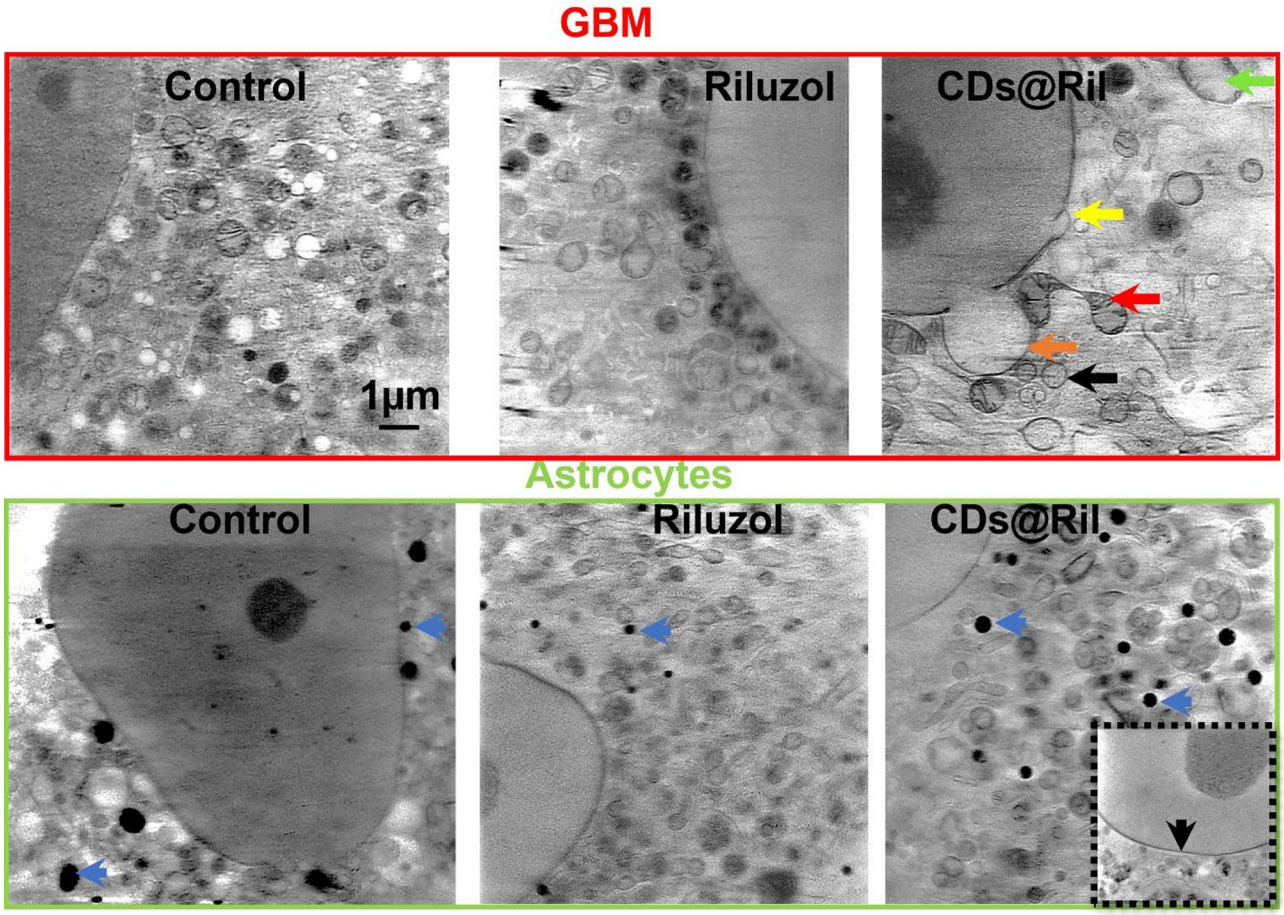

Fig. 8 Soft X-ray microscopy of control, riluzole and AMPS-CDs@RZ treated GBM cells and healthy astrocytes. The red arrow points to the mitochondria, the yellow nuclear membrane, the orange one the blebs and the black vesicles in the GBM cell. The blue arrow indicates lipid droplets in astrocyte cells. Insert (in black) and black arrow highlight intact nucleus membrane in astrocytes after AMPS-CD@RZ treatment

treatment. This imaging technique allowed us to visualise the endoplasmic reticulum (ER), mitochondria, and nuclear envelope (NE) in near-native conditions, highlighting significant structural changes in GBM cells.

The most important observation was the induction of NE blebbing in GBM cells treated with AMPS-CDs@RZ. NE blebbing, a hallmark of mechanical stress, often results in lamina disassembly and NE rupture. This phenomenon is linked to nuclear fragility, as nuclear envelope blebs typically arise from significant mechanical stress, leading to the disassembly of the nuclear lamina [53]. This phenomenon can lead to the uncontrolled mixing of nuclear and cytoplasmic contents, DNA damage, and activation of apoptotic pathways. Nuclear blebbing involves the formation of membrane-bound, spherical protrusions or bulges from the nuclear envelope, a process driven by the breakdown of the nuclear lamina [54]. While NE stress is a feature of several health issues, including cancer and premature ageing disorders, where the progressive enlargement of blebs underscores the pathological significance of NE stress, its precise mechanisms remain poorly understood [55]. Several proteins involved in NE reassembly after mitosis have been identified as repair factors, but the regulatory mechanisms controlling NE repair efficiency are not yet fully understood. Rapidly proliferating cancer cells often exhibit heightened NE stress responses, potentially linked to dysregulated cell cycle progression [55].

Our findings suggest that AMPS-CDs@RZ amplifies riluzole-induced toxicity in GBM cells by exacerbating NE stress, causing apoptosis and necroptosis. The molecular mechanism of the nuclear membrane disassembly and blebbing is the main way in apoptosis and necroptosis (reviewed in [54]). The observed changes in protein conformation, coupled with nuclear deformation, point to a possible mechanism involving protein misfolding stress signals that activate apoptosis. To the best of our knowledge, the involvement of this pathway in glioblastoma drug toxicity is undescribed and warrants further exploration not only as a potential target for glioblastoma therapy but also as a key cell biology matter to be addressed.

AMPS-CDs@RZ treatment also altered mitochondrial dynamics specifically in GBM cells but not in astrocytes, causing mitochondrial swelling and increased network fusion. Stress-induced mitochondrial hyper-fusion (SIMH) has been reported in response to diverse stressors, including ultraviolet radiation, nutrient deprivation and reactive oxygen species (ROS) (reviewed in [56]). These changes may reflect an adaptive response to maintain mitochondrial function under duress or a precursor to apoptotic signalling.

The ER also underwent significant remodelling in GBM- but not in astrocyte cells treated with AMPS-CDs@RZ, underscoring the interconnectedness of organelle function in stress responses to treatment of GBM. Mitochondrial-ER and mitochondrial-nuclear interactions are critical for maintaining cellular homeostasis and mediating apoptotic signals. It is known that mitochondria are often associated with other membranes, which are associations between the mitochondria and other organelles, such as ER, lysosomes, and peroxisomes (reviewed in [57, 58]). Mitochondria release pro-apoptotic factors, such as cytochrome c, in stress response, which can trigger caspase activation and subsequent apoptosis by influencing the nucleus or initiating autophagic processes[58–60]. Apoptosis and necroptosis are two major forms of regulated cell death, both involving significant changes to the nuclear and cellular membranes. In apoptosis, internal organelles are enclosed in membrane-bound vesicles to prevent inflammation. In necroptosis, large pores form in the cell membrane [54].

Furthermore, the increased vesicle formation observed in GBM cells suggests a mechanism of cellular response to toxicity. Vesicles may export cytotoxic compounds as a mechanism to resist toxicity [61–66] while simultaneously spreading cytotoxic agents to neighbouring cells *via* exosome-like structure molecules. These processes underscore the complex interplay between cellular defence mechanisms and drug-induced stress, which can be leveraged to enhance therapeutic outcomes.

Implications for cancer therapy

Our findings provide valuable insights into the cellular pathways mediating the cytotoxic effects of AMPS-CD@RZ in glioblastoma cells. While riluzole's anti-cancer effects—such as modulation of protein translation, oxidative stress induction, and DNA damage—are well-documented [36], its precise molecular mechanisms in glioblastoma remain unclear. The structural changes observed in glioblastoma cells following AMPS-CDs@RZ treatment, particularly nuclear envelope (NE) blebbing, altered mitochondrial dynamics, and increased vesicular trafficking, suggest these processes play key roles in its cytotoxicity.

Our data highlight the improved effects of riluzole combined with AMPS-CDs in targeting glioblastoma cells. The intracellular alterations point to a multifaceted mechanism of action that enhances the cytotoxicity of riluzole. These findings underscore the potential of the combined effect of AMPS-CDs and riluzole as a nanotherapeutic agent for glioblastoma therapy, particularly in tumors resistant to conventional treatments.

The results show that the AMPS-CD nanoparticles markedly enhance riluzole's biological activity in patient-derived primary glioblastoma cultures, likely through a synergistic interaction. While these findings are promising, further validation in physiologically relevant systems

is needed. As a next step, ongoing experiments using 3D glioblastoma cell culture are underway to evaluate therapeutic efficacy in a more complex tumor microenvironment. Interpreting the activity of polyionic nanocarriers presents challenges due to the dynamic equilibrium between free and nanoparticle-bound drug species. Under tightly controlled experimental conditions, specifically temperature, pH, and pressure, the AMPS@Rz complex appears to be the predominant contributor to the observed effects, with minimal equilibrium shift, consistent with Le Châtelier's Principle. Future studies should focus on elucidating the release kinetics, structural stability, and molecular interactions of the nanocarrier system to further refine its therapeutic potential and inform rational design strategies for glioblastoma treatment.

Importantly, AMPS-CDs reduced riluzole toxicity in non-tumor astrocytes, preserving their structural integrity and mitigating lipid peroxidation. This selectivity suggests that AMPS-CDs can minimise collateral damage to healthy brain tissue, addressing a major limitation of current glioblastoma therapies.

Supplementary data

Supplementary data to this article can be found online.

- Summarized relative cell viability of healthy after treatment with different concentrations of riluzole (RZ), *AMPS-CDs* NPs (No RZ group), and AMPS-CDs@RZ is presented in Figure S1).
- The live cell FTIR assay on the GBM and astrocytes treated with riluzole drug, without the NPs (Figure S2 and S3).
- The PCA analysis of the Amide I and Amide II region of the FTIR spectra of GBM and astrocyte cells is shown in Figures S4 and S5, respectively.
- Reconstructed SXT videos of single cells chartography could be found in Supplemental data.

Conclusions

This study demonstrates that AMPS-CDs nanoparticles significantly enhance the therapeutic efficacy of riluzole in GBM cells, as revealed by SXT advanced in situ imaging and live-cell μFTIR spectroscopic analyses. The AMPS-CDs@RZ treatment induced profound structural and biochemical changes, including nuclear envelope blebbing, mitochondrial hyper-fusion, and increased vesicle formation, leading to targeted GBM cell death while sparing non-tumor astrocytes. Synchrotron-based FTIR spectroscopy revealed specific increased effects of AMPS-CDs@RZ treatment, influencing DNA integrity, protein conformation, and lipid metabolism. Notably, alterations in protein secondary structures, including changes in glutamate levels and α-helix configurations, were observed in glioblastoma cells. AMPS-CDs, however, preserved protein stability in astrocytes, maintaining α-helix and β-sheet structures akin to untreated controls. Furthermore, AMPS-CDs@RZ treatment exacerbated lipid peroxidation and disrupted intracellular membranes in glioblastoma cells, while normalising these parameters in healthy astrocytes. The novel involvement of nuclear envelope blebbing in riluzole-induced glioblastoma toxicity provides new mechanistic insights into cancer cell stress responses. Our findings underscore the potential of AMPS-CDs to enhance the selective efficacy of riluzole while mitigating its effects on healthy tissue. Future in vivo studies will further explore this promising nanotherapeutic platform for glioblastoma therapy.

Supplementary Information

The online version contains supplementary material available at https://doi.org/10.1186/s12951-025-03687-2.

Supplementary Material 1.

Supplementary Material 2.

Supplementary Material 3.

Acknowledgements

The authors are thankful for financial support MCIN/AEI/https://doi.org/10.13039/501100011033 through the project PID2021-122613OB-I00 and Universidad de Máálaga ref. IEDI-Proyecto11-2022-RYC2014-15410. TD is grateful to the ALBA in-house grant: "Synergetic multimodal FTIR and X-ray spectro-microscopical approach for 3D cell culture evaluation". These experiments were performed at the MIRAS and MISTRAL beamlines at the ALBA Synchrotron projects IH 2024058465 and 2024028082. We thank Jessica do Nascimento Faria for the assistance during the cell freezing preparation.

Author contributions

Conceptualization: TD; Investigation: TD, EGM, EP, CFG, MN, SS, MA; Formal analysis: TD, EGM, EP; Visualization: TD; Writing - original draft: TD; Writing - review & editing: all authors. All authors read and approved the final manuscript.

Funding

MCIN/AEI/https://doi.org/10.13039/501100011033 through the project PID2021-122613OB-I00 and Universidad de Máálaga ref.IEDI-Proyecto11-2022-RYC2014-15410 and ALBA in-house grant: "Synergetic multimodal FTIR and X-ray spectro-microscopical approach for 3D cell culture evaluation".

Data availability

Data is provided within the manuscript or supplementary information files have been deposited in ALBA Synchrotron light facility.

Declarations

Ethics approval

For this study was unwaveringly obtained from the Ethics Committee of the esteemed University Medical Center Göttingen, Germany (approval number 11/8/13).

Competing interests

The authors declare no competing interests.

Author details

[1]ALBA Synchrotron light source, Carrer de la Llum 2-26, 08290 Cerdanyola del Vallès, Barcelona, Spain

[2]The Translational Neurooncology Research Group, Department of Neurosurgery, University Medical Center Göttingen, Robert-Koch-Strasse 40, 37075 Göttingen, Germany
[3]INAMAT2 - Institute for Advanced Materials and Mathematics, Department of Science, Public University of Navarra. Campus de Arrosadia, Pamplona 31006, Spain
[4]Instituto de Investigación Biomédica de Málaga y Plataforma en Nanomedicina-IBIMA Plataforma BIONAND, Málaga, Spain
[5]Department of Cell Biology, Genetics and Physiology, Universidad de Málaga, Málaga, Spain

Received: 5 December 2024 / Accepted: 23 August 2025
Published online: 06 October 2025

References

1. Lee JH, Lee JE, Kahng JY, Kim SH, Park JS, Yoon SJ, et al. Human glioblastoma arises from subventricular zone cells with low-level driver mutations. Nature. 2018. https://doi.org/10.1038/s41586-018-0389-3.
2. Louis DN, Perry A, Reifenberger G, von Deimling A, Figarella-Branger D, Cavenee WK, et al. The 2016 World Health Organization classification of tumors of the central nervous system: a summary. Acta Neuropathol. 2016. https://doi.org/10.1007/s00401-016-1545-1.
3. Ray SK. *Glioblastoma. Molecular Mechanisms of Pathogenesis and Current Therapeutic Strategies*; Ray, S. K., Ed.; 2010. https://doi.org/10.1007/978-1-4419-0410-2
4. Surowka AD, Adamek D, Szczerbowska-Boruchowska M. The combination of artificial neural networks and synchrotron radiation-based infrared microspectroscopy for a study on the protein composition of human glial tumors. Analyst. 2015;140(7):2428–38. https://doi.org/10.1039/c4an01867b.
5. Han S-P, Kim J-H, Han M-E, Sim H-E, Kim K-S, Yoon S, Baek S-Y, Kim B-S, Oh S-O. SNAI1 is involved in the proliferation and migration of glioblastoma cells. Cell Mol Neurobiol. 2011;31(3):489–96. https://doi.org/10.1007/s10571-010-9643-4.
6. Din FU, Aman W, Ullah I, Qureshi OS, Mustapha O, Shafique S, et al. Effective use of nanocarriers as drug delivery systems for the treatment of selected tumors. Int J Nanomedicine. 2017. https://doi.org/10.2147/IJN.S146315.
7. Algarra M, Soto J, Soledad Pino-González M, Gonzalez-Munoz E, Dučić T. Multifunctionalized carbon Dots as an active nanocarrier for drug delivery to the glioblastoma cell line. ACS Omega. 2024;0(0). https://doi.org/10.1021/acsomega.3c08459.
8. Liu J, Wang L-N. The efficacy and safety of riluzole for neurodegenerative movement disorders: a systematic review with meta-analysis. Drug Deliv. 2018;25(1):43–8. https://doi.org/10.1080/10717544.2017.1413446.
9. Armando R, Mengual Gómez D, Gomez D. New drugs are not enoughdrug repositioning in oncology: an update. Int J Oncol. 2020. https://doi.org/10.3892/ijo.2020.4966.
10. Seol HS, Lee SE, Song JS, Lee HY, Park S, Kim I, et al. Glutamate release inhibitor, riluzole, inhibited proliferation of human hepatocellular carcinoma cells by elevated ROS production. Cancer Lett. 2016;382(2):157–65. https://doi.org/10.1016/j.canlet.2016.08.028.
11. Sun L, Wu C, Ming J, Nie X, Guo E, Zhang W, Hu G. Riluzole enhances the response of human nasopharyngeal carcinoma cells to ionizing radiation via ATM/P53 signalling pathway. J Cancer. 2020;11(11):3089–98. https://doi.org/10.7150/jca.41217.
12. Wall BA, Yu LJ, Khan A, Haffty B, Goydos JS, Chen S. Riluzole is a radiosensitizing agent in an in vivo model of brain metastasis derived from GRM1 expressing human melanoma cells. Pigment Cell Melanoma Res. 2015. https://doi.org/10.1111/pcmr.12327.
13. Brandao M, Simon T, Critchley G, Giamas G. Astrocytes, the rising stars of the glioblastoma microenvironment. Glia. 2019. https://doi.org/10.1002/glia.23520.
14. Dučić T, Ninkovic M, Martínez-Rovira I, Sperling S, Rohde V, Dimitrijević D, et al. Live-cell synchrotron-based FTIR evaluation of metabolic compounds in brain glioblastoma cell lines after riluzole treatment. Anal Chem. 2022;94(4):1932–40. https://doi.org/10.1021/acs.analchem.1c02076.
15. Wehbe K, Travo A, Eimer S, Cinque G, Barron E, Déléris G, et al. Investigation of blood vessels in glioblastoma at a micrometric scale: a comparative study by synchrotron and conventional micro-FTIR. Anal Methods. 2013;5(24):6925. https://doi.org/10.1039/c3ay41449c.
16. Sandt C, Nadaradjane C, Richards R, Dumas P, Sée V. Use of infrared microspectroscopy to elucidate a specific chemical signature associated with hypoxia levels found in glioblastoma. Analyst. 2016;141(3):870–83. https://doi.org/10.1039/C5AN02112J.
17. Kenig S, Bedolla DE, Birarda G, Faoro V, Mitri E, Vindigni A, Storici P, Vaccari L. Fourier transform infrared microspectroscopy reveals biochemical changes associated with glioma stem cell differentiation. Biophys Chem. 2015;207:90–6. https://doi.org/10.1016/J.BPC.2015.09.005.
18. López-Lorente ÁI, Mizaikoff B. Recent advances on the characterization of nanoparticles using infrared spectroscopy. TRAC Trends Anal Chem. 2016;84:97–106. https://doi.org/10.1016/j.trac.2016.01.012.
19. Toplak M, Birarda G, Read S, Sandt C, Rosendahl SM, Vaccari L, Demšar J, Borondics F. Infrared orange: connecting hyperspectral data with machine learning. Synchrotron Radiat News. 2017;30(4):40–5. https://doi.org/10.1080/08940886.2017.1338424.
20. Demšar J, Curk T, Erjavec A, Gorup Č, Hočevar T, Milutinovič M, Možina M, Polajnar M, Toplak M, Starič A, Štajdohar M, Umek L, Žagar L, Žbontar J, Žitnik M, Zupan B. Orange: data mining toolbox in python. J Mach Learn Res. 2013;14:2349–53.
21. Vaccari L, Birarda G, Businaro L, Pacor S, Grenci G. Infrared microspectroscopy of live cells in microfluidic devices (MD-IRMS): toward a powerful label-free cell-based assay. Anal Chem. 2012;84(11):4768–75. https://doi.org/10.1021/ac300313x.
22. Pascual-Izarra C, Cuní G, Falcón-Torres C, Fernández-Carreiras D, Reszela Z, Rosanes M. EFFORTLESS CREATION OF CONTROL & DATA ACQUISITION GRAPHICAL USER INTERFACES WITH TAURUS. In *Proceedings of ICALEPCS2015, Melbourne, Australia*; 2015; pp 1138–1142.
23. Groen J, Sorrentino A, Aballe L, Oliete R, Valcárcel R, Okolo C, Kounatidis I, Harkiolaki M, Pérez-Berná AJ, Pereiro E. A 3D cartographic description of the cell by cryo soft X-Ray tomography. J Visualized Experiments. 2021;2021(169). https://doi.org/10.3791/62190.
24. González-Larraza PG, López-Goerne TM, Padilla-Godínez FJ, González-López MA, Hamdan-Partida A, Gómez E. IC50 evaluation of platinum nanocatalysts for cancer treatment in fibroblast, Hela, and DU-145 cell lines. ACS Omega. 2020. https://doi.org/10.1021/acsomega.0c03759.
25. Sperling S, Aung T, Martin S, Rohde V, Ninkovic M. Riluzole. A potential therapeutic intervention in human brain tumor stem-like cells. Oncotarget. 2017;8(57):96697–709. https://doi.org/10.18632/oncotarget.18043.
26. Dučić T, Paunesku T, Chen S, Ninković M, Speling S, Wilke C, et al. Structural and elemental changes in glioblastoma cells: in situ: complementary imaging with high resolution visible light- and x-ray microscopy. Analyst. 2017;142(2):356–65. https://doi.org/10.1039/c6an02532c.
27. Malek K, Wood BR, Bambery KR. FTIR imaging of tissues: techniques and methods of analysis. Optical spectroscopy and computational methods in biology and medicine. Springer Netherlands: Dordrecht,; 2014. pp. 419–73. https://doi.org/10.1007/978-94-007-7832-0_15.
28. De Meutter J, Goormaghtigh E. Amino acid side chain contribution to protein FTIR spectra: impact on secondary structure evaluation. Eur Biophys J. 2021;50:3–4. https://doi.org/10.1007/s00249-021-01507-7.
29. Pal MM. Glutamate. The master neurotransmitter and its implications in chronic stress and mood disorders. Front Hum Neurosci. 2021. https://doi.org/10.3389/fnhum.2021.722323.
30. Ankarcrona M, Dypbukt JM, Bonfoco E, Zhivotovsky B, Orrenius S, Lipton SA, et al. Glutamate-induced neuronal death: a succession of necrosis or apoptosis depending on mitochondrial function. Neuron. 1995. https://doi.org/10.1016/0896-6273(95)90186-8.
31. Inouye M, Mio T, Sumino K. Formation of 9-hydroxy linoleic acid as a product of phospholipid peroxidation in diabetic erythrocyte membranes. Biochim Biophys Acta. 1999;1438(2):204–12.
32. Rodríguez-Casado A, Alvarez I, Toledano A, de Miguel E, Carmona P. Amphetamine effects on brain protein structure and oxidative stress as revealed by FTIR microspectroscopy. Biopolymers. 2007;86(5–6):437–46. https://doi.org/10.1002/bip.20753.
33. Kreuzer M, Dučić T, Hawlina M, Andjelic S. Synchrotron-based FTIR. microspectroscopy of protein aggregation and lipids peroxidation changes in human cataractous lens epithelial cells. Sci Rep. 2020. https://doi.org/10.1038/s41598-020-72413-9.
34. Clède S, Lambert F, Sandt C, Gueroui Z, Delsuc N, Dumas P, et al. Synchrotron radiation FTIR detection of a metal-carbonyl Tamoxifen analog. Correlation with luminescence microscopy to study its subcellular distribution. Biotechnol Adv. 2013. https://doi.org/10.1016/j.biotechadv.2012.01.023.

35. Lemieszek MK, Stepulak A, Sawa-Wejksza K, Czerwonka A, Ikonomidou C, Rzeski W. Riluzole inhibits proliferation, migration and cell cycle progression and induces apoptosis in tumor cells of various origins. Anticancer Agents Med Chem. 2018;18(4). https://doi.org/10.2174/1871520618666180228152713.
36. Blyufer A, Lhamo S, Tam C, Tariq I, Thavornwatanayong T, Mahajan SS, Riluzole. A neuroprotective drug with potential as a novel Anti-Cancer agent (Review). Int J Oncol. 2021. https://doi.org/10.3892/IJO.2021.5275.
37. Yelskaya Z, Carrillo V, Dubisz E, Gulzar H, Morgan D, Mahajan SS. Synergistic inhibition of survival, proliferation, and migration of U87 cells with a combination of LY341495 and Iressa. PLoS ONE. 2013;8(5):e64588. https://doi.org/10.1371/journal.pone.0064588.
38. Sachkova A, Sperling S, Mielke D, Schatlo B, Rohde V, Ninkovic M. Combined applications of repurposed drugs and their detrimental effects on glioblastoma cells. Anticancer Res. 2019;39(1):207–14. https://doi.org/10.21873/anticanres.13099.
39. Willard SS, Koochekpour S. Glutamate signaling in benign and malignant disorders: current status, future perspectives, and therapeutic implications. Int J Biol Sci. 2013;9(7):728. https://doi.org/10.7150/ijbs.6475.
40. Richter JM, Schaefer M, Hill K. Riluzole activates TRPC5 channels independently of PLC activity. Br J Pharmacol. 2014;171(1):158. https://doi.org/10.1111/bph.12436.
41. De La Ballina LR, Cano-Crespo S, González-Muñoz E, Bial S, Estrach S, Cailleteau L, et al. Amino acid transport associated to cluster of differentiation 98 heavy chain (CD98HC) is at the cross-road of oxidative stress and amino acid availability. J Biol Chem. 2016. https://doi.org/10.1074/jbc.M115.704254.
42. Lin W, Wang C, Liu G, Bi C, Wang X, Zhou Q, Jin H. SLC7A11/XCT in cancer: biological functions and therapeutic implications. Am J Cancer Res 2020, *10* (10).
43. de Groot J, Sontheimer H. Glutamate and the biology of gliomas. Glia. 2011. https://doi.org/10.1002/glia.21113.
44. Savaskan NE, Heckel A, Hahnen E, Engelhorn T, Doerfler A, Ganslandt O, et al. Small interfering RNA-mediated XCT silencing in gliomas inhibits neurodegeneration and alleviates brain edema. Nat Med. 2008;14(6):629. https://doi.org/10.1038/nm1772.
45. Alberts B, Johnson A, Lewis J, Morgan D, Raff M, Roberts K, Walter P. *Molecular Biology of the Cell*; 2017. https://doi.org/10.1201/9781315735368
46. Hansen KB, Wollmuth LP, Bowie D, Furukawa H, Menniti FS, Sobolevsky AI, et al. Structure, function, and pharmacology of glutamate receptor ion channels. Pharmacol Rev. 2021. https://doi.org/10.1124/pharmrev.120.000131.
47. Gaschler MM, Stockwell BR. Lipid peroxidation in cell death. Biochem Biophys Res Commun. 2017. https://doi.org/10.1016/j.bbrc.2016.10.086.
48. Roy SK, Ma Y, Lam BQ, Shrivastava A, Srivastav S, Shankar S, et al. Riluzole regulates pancreatic cancer cell metabolism by suppressing the Wnt-β-catenin pathway. Sci Rep. 2022. https://doi.org/10.1038/s41598-022-13472-y.
49. Rådmark O, Werz O, Steinhilber D, Samuelsson B. 5-Lipoxygenase, a key enzyme for leukotriene biosynthesis in health and disease. Biochimica et Biophysica Acta (BBA). 2015. https://doi.org/10.1016/j.bbalip.2014.08.012.
50. Ackermann JA, Hofheinz K, Zaiss MM, Krönke G. The double-edged role of 12/15-lipoxygenase during inflammation and immunity. Biochim Et Biophys Acta - Mol Cell Biology Lipids. 2017. https://doi.org/10.1016/j.bbalip.2016.07.014.
51. Chen CT, Green JT, Orr SK, Bazinet RP. Regulation of brain polyunsaturated fatty acid uptake and turnover. Prostaglandins Leukot Essent Fatty Acids. 2008;79:3–5. https://doi.org/10.1016/j.plefa.2008.09.003.
52. Villalón-García I, Povea-Cabello S, Álvarez-Córdoba M, Talaverón-Rey M, Suárez-Rivero JM, Suárez-Carrillo A, et al. Vicious cycle of lipid peroxidation and iron accumulation in neurodegeneration. Neural Regen Res. 2023. https://doi.org/10.4103/1673-5374.358614.
53. Srivastava N, Nader GP, de Williart F, Rollin A, Cuvelier R, Lomakin D, Piel A. Nuclear fragility, blaming the blebs. Curr Opin Cell Biol. 2021. https://doi.org/10.1016/j.ceb.2021.01.007.
54. Lee GE, Byun J, Lee CJ, Cho YY. Molecular mechanisms for the regulation of nuclear membrane integrity. Int J Mol Sci. 2023. https://doi.org/10.3390/ijms242015497.
55. Kamikawa Y, Wu Z, Nakazawa N, Ito T, Saito A, Imaizumi K. Impact of cell cycle on repair of ruptured nuclear envelope and sensitivity to nuclear envelope stress in glioblastoma. Cell Death Discov. 2023. https://doi.org/10.1038/s41420-023-01534-7.
56. Meyer JN, Leuthner TC, Luz AL. Mitochondrial fusion, fission, and mitochondrial toxicity. Toxicology. 2017. https://doi.org/10.1016/j.tox.2017.07.019.
57. Walker BR, Moraes CT. Nuclear-mitochondrial interactions. Biomolecules. 2022. https://doi.org/10.3390/biom12030427.
58. Zhang Y, Wu Y, Zhang M, Li Z, Liu B, Liu H, et al. Synergistic mechanism between the endoplasmic reticulum and mitochondria and their crosstalk with other organelles. Cell Death Discov. 2023. https://doi.org/10.1038/s41420-023-01353-w.
59. Nguyen TT, Wei S, Nguyen TH, Jo Y, Zhang Y, Park W, et al. Mitochondria-associated programmed cell death as a therapeutic target for age-related disease. Exp Mol Med. 2023. https://doi.org/10.1038/s12276-023-01046-5.
60. Shimura T. Mitochondrial signaling pathways associated with DNA damage responses. Int J Mol Sci. 2023. https://doi.org/10.3390/ijms24076128.
61. Bandari SK, Purushothaman A, Ramani VC, Brinkley GJ, Chandrashekar DS, Varambally S, et al. Chemotherapy induces secretion of exosomes loaded with heparanase that degrades extracellular matrix and impacts tumor and host cell behavior. Matrix Biol. 2018. https://doi.org/10.1016/j.matbio.2017.09.001.
62. Pascucci L, Coccè V, Bonomi A, Ami D, Ceccarelli P, Ciusani E, Viganò L, Locatelli A, Sisto F, Doglia SM, Parati E, Bernardo ME, Muraca M, Alessandri G, Bondiolotti G, Pessina A. Paclitaxel Is Incorporated by Mesenchymal Stromal Cells and Released in Exosomes That Inhibit in Vitro Tumor Growth: A New Approach for Drug Delivery. *Journal of Controlled Release* 2014, *192*. https://doi.org/10.1016/j.jconrel.2014.07.042
63. Lv LH, Wan YL, Lin Y, Zhang W, Yang M, Li GN, Lin HM, Shang CZ, Chen YJ, Min J. Anticancer drugs cause release of exosomes with heat shock proteins from human hepatocellular carcinoma cells that elicit effective natural killer cell antitumor responses in vitro. J Biol Chem. 2012;287(19). https://doi.org/10.1074/jbc.M112.340588.
64. Ab Razak NS, Ab Mutalib NS, Mohtar MA, Abu N. Impact of chemotherapy on extracellular vesicles: understanding the Chemo-EVs. Front Oncol. 2019. https://doi.org/10.3389/fonc.2019.01113.
65. Shedden K, Xie XT, Chandaroy P, Chang YT, Rosania GR. Expulsion of small molecules in vesicles shed by cancer cells: association with gene expression and chemosensitivity profiles. Cancer Res. 2003;63:15.
66. Safaei R, Larson BJ, Cheng TC, Gibson MA, Otani S, Naerdemann W, et al. Abnormal lysosomal trafficking and enhanced exosomal export of cisplatin in drug-resistant human ovarian carcinoma cells. Mol Cancer Ther. 2005. https://doi.org/10.1158/1535-7163.MCT-05-0102.

Publisher's note